Available online at www.sciencedirect.com
SCIENCE DIRECT®
Earth and Planetary Science Letters 239 (2005) 9–17
EPSL
www.elsevier.com/locate/epsl

Mapping the subducting Pacific slab beneath southwest Japan with Hi-net receiver functions

Fenglin Niu [a], Alan Levander [a,*], Sangwon Ham [a], Masayuki Obayashi [b]

[a] *Department of Earth Science, MS-126, Rice University, 6100 Main St., Houston, TX 77005, USA*
[b] *IFREE, Japan Marine Science and Technology Center, Yokosuka, Japan*

Received 11 May 2005; received in revised form 9 August 2005; accepted 11 August 2005
Available online 22 September 2005
Editor: S. King

Abstract

We have used 4th root receiver function stacks, and pre-stack receiver function depth migrations to study the transition zone discontinuity structure beneath southwestern Japan. Receiver functions were calculated from the quiet short-period seismograms recorded by a recently deployed borehole network, Hi-net. We found that a relatively broad frequency band can be retrieved from a short-period seismogram by a deconvolution of the instrument response. The quality of the receiver functions formed from large earthquake recordings is comparable to those from broadband instruments. We applied common-conversion-point gathering to the receiver-function data to image the P to S conversion events beneath the network by stacking with a 4th root technique to improve lateral coherence. We found that the topographic anomalies of the 410- and 660-km discontinuities beneath southwest Japan have very different length scales. The former is characterized by a narrow, ~150–200 km wide, topographic high, while the latter exhibits a broad, >400 km wide, moderate topographic low together with a small-scale, larger-amplitude depression. A 2.5D pre-stack depth migration of the receiver functions shows the transition zone features clearly, as well as images of a change of slope in the subducting slab at the 410 discontinuity and flattening of the slab onto the 660-km. These observations show that the subducted Pacific slab is deflected when it encounters the upper and lower boundaries of the transition zone, and is flat lying either above or across the 660-km discontinuity. The flat lying slab is, however, restricted to the bottom of the transition zone, and probably experiences much less thickening than is suggested by some global tomographic images in which subhorizontal high velocity anomalies are seen throughout the transition zone between the two discontinuities.

Keywords: mantle discontinuities; phase transition; receiver function; subduction zone; southwest Japan

1. Introduction

Seismic observations of the two mantle discontinuities at 410 and 660 km depth are essential for studying the dynamics and mineral physics of the mantle, in particular images of subducting slabs interacting with the transition zone discontinuities are used to infer whether convection involves the whole mantle or is partitioned into upper and lower mantle cells. For example, the extension of high velocity anomalies across the 660-km discontinuity in some subduction regimes in global tomographic images [1–5] has been taken as direct evidence of slab penetration into the lower mantle, changing a long held view of the discontinuity as a boundary that separates geochemical reservoirs and

* Corresponding author. Tel.: +1 713 348 6064; fax: +1 713 348 5214.
E-mail address: alan@rice.edu (A. Levander).

0012-821X/$ - see front matter © 2005 Elsevier B.V. All rights reserved.
doi:10.1016/j.epsl.2005.08.009

isolates the lower mantle from plate tectonic mixing [6]. Global tomographic images, on the other hand, also show that some of the subducting slabs lie flat on the 660-km discontinuity or pile up within the top of the lower mantle. Thus tomographic images have been interpreted very differently in terms of their implications for mantle convection. Some of the controversy arises from the limitations in lateral and vertical resolution of tomographic images, and requires other seismic techniques to resolve them. To study the interactions between subducting slabs and the 660-km discontinuity, another commonly used technique is to map the slab-induced deflection of the discontinuity. As the 660-km discontinuity is generally believed to be caused by a temperature sensitive phase change observed in experimental studies of olivine, the major mineral component in the upper mantle [7], a temperature induced depression of the 660-km is expected to occur in a broad area for a subhorizontally deflected slab whereas it will occur in a narrow region for a continuously sinking slab.

One ideal location to study the interaction between a subducting slab and the 660-km discontinuity is in northeastern China and Japan where the subducting Pacific lithosphere can be traced back to the Japan Trench from seismicity, which has been well located by the large number of seismographs located there (Fig. 1). Fukao et al. [1] found that the subducted Pacific slab is deflected subhorizontally around the 660-km discontinuity beneath a large part of northeastern China (Fig. 1). A large-scale depression of the 660-km discontinuity is observed from SS precursor data in the same region [8,9]. Due to the low lateral resolution of the SS precursor, it has been argued that the real anomaly might be much smaller in scale [10]. Shearer et al. [11] later found that small-scale structure on the 660-km discontinuity near subducting slabs would not cause significant bias in maps of large-scale 660-km topography derived from long-period SS precursor observations. Niu and Kawakatsu [12,13] used P to S converted data to determine the absolute depth of the 410- and 660-km discontinuities in this region. A multi-discontinuity structure was found at the tip of the subducting slab and was interpreted as phase transitions associated with the garnet component of the upper mantle [14]. A thick transition zone was observed at the CDSN (Chinese Digital Seismic Network) station BJI (Fig. 1), which was taken as evidence supporting the view of a stagnant slab lying around the 660-km. In addition to the broad depression associated with the flat lying slab (red rectangle in Fig. 1a), recent receiver-function images also found that significant topography of the

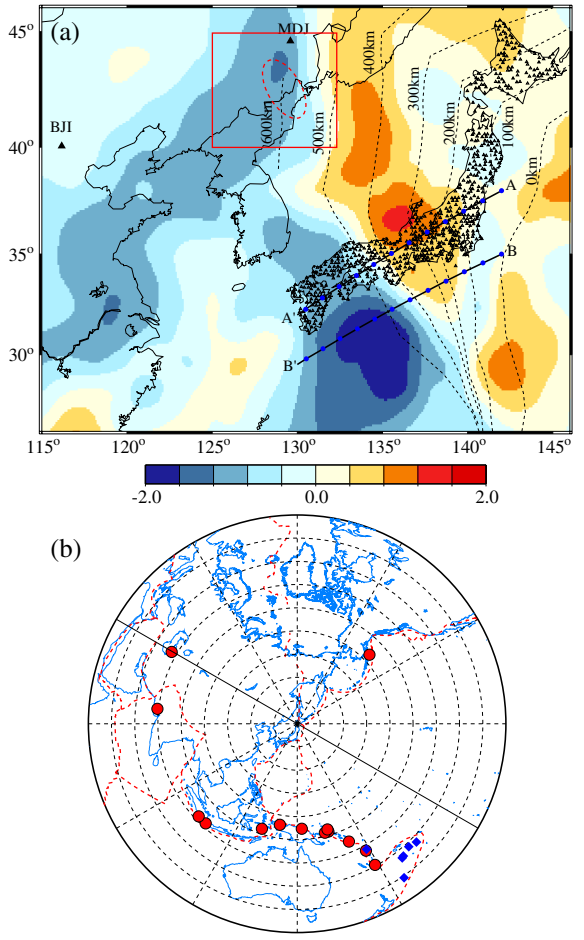

Fig. 1. (a) Map showing part of the northwest Pacific subduction zone. The Wadati–Benioff zone is indicated by black dashed lines. Open triangles show the locations of the Hi-net stations. The two solid black lines are the locations of the two sections shown in Fig. 5. The two filled triangles are the CDSN stations BJI and MDJ mentioned in the text. Red rectangle roughly shows the region studied by Ai et al. [15] and Li and Yuan [16], and the ellipse indicates the region where significant depression of the 660-km discontinuity is observed. P-wave tomographic model of Fukao et al. [5] for the lower transition zone layer (629–712 km) are shown by a color contour. (b) Distribution of the 20 earthquakes used in this study. Earthquakes that occurred at depths shallower and deeper than 50 km are respectively shown in red circles and blue diamonds.

660-km discontinuity exists only within a relatively small area near the border between China and North Korea (dashed ellipse in Fig. 1a) [15,16], suggesting a complicated picture of subduction processes in this region.

In this study, we have investigated another section of the Pacific subduction zone, in southwestern Japan, where the subducting slab is also found to extend subhorizontally along the upper and lower mantle transition regions [1,5]. Unlike northeastern China, where data from a network of only ~20 stations are available,

southwestern Japan is covered well by over 300 borehole seismic stations. The dense coverage allows us to image at relatively small scale the topographic anomalies of the two transition zone discontinuities.

2. Data and analysis

The data we used in this study were recorded by a recently installed borehole seismic network, the High Sensitivity Seismograph Network (Hi-net). The network consists of about 700 three-component short-period seismographs that cover all the Japanese islands (Fig. 1a). The network started recording data in August, 2000.

Receiver functions are usually calculated by a deconvolution of the radial (R) component by the vertical component (Z) of teleseismic recordings [17,18]. The deconvolution can be performed either in the time or frequency domain. In this study we adopted the latter. A water level is set to avoid instability arising from division of the R-spectrum by the Z-spectrum [19,20]. The Hi-net sensors have a natural frequency of about 1 Hz, and the frequency band of recording is quite narrow. Much of the low frequency content is below the water level. Deconvolution with the raw short-period velocity records thus results in very poor-quality receiver functions.

The typical frequency response for a Hi-net sensor to ground velocity can be simplified as [21]:

$$I(\omega) = \frac{G\omega^2}{-\omega^2 + 2ih\omega_0\omega + \omega_0^2}, \quad (1)$$

where ω_0 is the natural frequency of the sensor ($2\pi \times 1$ Hz), h is the damping constant (0.7) and G is the gain factor. The above response serves as a high-pass filter. To restore the low frequency signals from the recordings, a deconvolution of velocity seismograms by the above instrument response was first implemented before the calculation of receiver functions, and then followed with a .02 Hz high-pass filter, extending the instrument response more than a decade at the low frequency end. Receiver functions derived from the above procedures are generally of good quality (Fig. 2a). Stacking these receiver functions clearly reveals two P to S conversion peaks at ~415 and 675 km (Fig. 2b).

We examined most of the teleseismic events that occurred in the period between August 2000 and January 2003. We found that long-period signals are well recovered and the signal-to-noise ratio of the corresponding receiver functions is high. 7903 receiver functions from 20 events were finally selected for

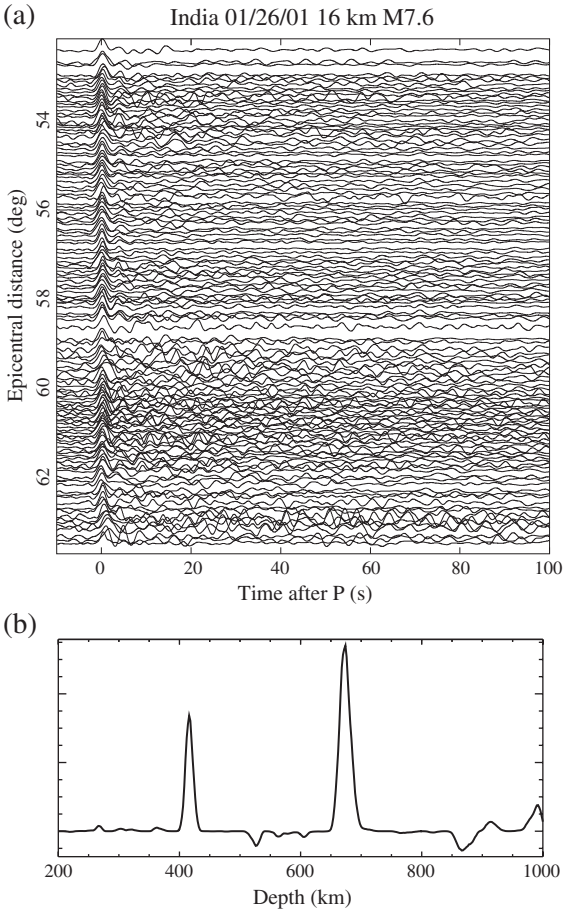

Fig. 2. An example of individual (a) and depth converted (b) receiver functions. The 410- and 660-km discontinuities are clearly shown in the depth converted trace. Arrival times of $P_{410}s$ and $P_{660}s$ predicted by *iasp91* are shown as dashed lines in (a). A 4th root stack and only the data from the India earthquake (event 12 in Table 1) are used in producing (b). Time-depth conversion is based on the *iasp91* model.

imaging with stacking methods. The moment magnitude of the 20 events varies from 6.3 to 7.8 and depth ranges from ~10 to ~630 km (Fig. 1b, Table 1). We used a source time window of 125 s (5 s before and 120 s after the P wave) in the deconvolution for generating receiver functions. The depth phases arriving in this time window are considered to be part of the source, allowing us to include data from two intermediate depth earthquakes. We set our imaging depth from 200 to 1000 km. Since $P_{1000}s$ arrives at ~100 s after P, a ~250 s time window of the R-component seismograms was used to calculate spectra to satisfy the deconvolution causality.

The conversion points at 410 and 660 km depths are plotted in Fig. 3a and b, respectively. The high quality of the data plus the dense coverage of the study region make it ideal for increasing signal to noise ratios by

Table 1
Event list

Event no.	Origin time (mm/dd/yy min/ss)	Lat. (°N)	Lon. (°E)	Depth (km)	Mw
1	08/28/00 15:05	−4.11	127.39	16.0	6.8
2	09/26/00 06:17	−17.18	−173.93	56.0	6.3
3	10/04/00 16:58	−15.42	166.91	23.0	6.9
4[a]	10/25/00 09:32	−6.55	105.63	38.0	6.8
5	11/17/00 21:01	−5.50	151.78	33.0	7.8
6	11/18/00 02:05	−5.10	153.18	33.0	6.6
7	12/06/00 17:11	39.57	54.80	30.0	7.0
8	12/06/00 22:57	−4.22	152.73	31.0	6.5
9	12/18/00 01:19	−21.18	−179.12	628.2	6.5
10	01/09/01 16:49	−14.93	167.17	103.0	7.0
11[a]	01/10/01 16:02	57.08	−153.21	33.0	6.9
12[a]	01/26/01 03:16	23.42	70.23	16.0	7.6
13[a]	02/13/01 19:28	−4.68	102.56	36.0	7.3
14	02/28/01 12:30	−21.99	170.21	10.0	6.7
15	04/28/01 04:49	−18.06	−176.94	351.8	6.8
16	06/03/01 02:41	−29.67	−178.63	178.1	7.1
17	08/19/02 11:01	−21.70	−179.51	580.0	7.6
18	09/08/02 18:44	−3.30	142.95	13.0	7.6
19	10/10/02 10:50	−1.76	134.30	10.0	7.5
20	01/20/03 08:43	−10.49	160.77	33.0	7.3

[a] Used for pre-stack depth migration.

common conversion point stacking procedures developed for receiver function imaging, in analogy to those developed for petroleum exploration [22–24]. For migration we selected a subset of 4 earthquakes whose back-azimuths from the Hi-net array are close to the local dip direction of the Wadati–Benioff zone beneath southwestern Japan (Fig. 1; Table 1).

2.1. Common conversion point stacking

For a conversion depth d, we first calculated the ray path of converted phase Pds and its arrival time relative to P by ray tracing the 1D *iasp91* velocity model [25]. Arrival time anomalies of P and Pds introduced by 3D velocity structure are further calculated using the whole mantle velocity model of [5]. The S-wave velocity model is made from the P-wave velocity by assuming *iasp91* V_p/V_s ratios. We used a bin size of $1^\circ \times 1^\circ$ for gathering the receiver functions. The number of receiver functions in each bin varies between 10 and 300 with an average of 80. We then summed the receiver functions and further averaged the summations within a 0.5 s window centered on the arrival time of Pds using an nth root stacking method [26,27]. We chose $n=4$ to reduce the uncorrelated noise relative to the usual linear stack ($n=1$), recognizing that this suppresses conversions with significant dip away from the horizontal. We varied d from 200 to 1000 km in increments of 10 km. The final CCP images are shown in Fig. 4.

2.2. Pre-stack receiver function depth migration

To image the dipping Pacific slab we used a 2.5D Kirchhoff pre-stack depth migration [28,29] to form an image from the receiver functions from 4 earthquakes (Table 1). To avoid 3D complexity, we have chosen 4 earthquakes that are located roughly along the azimuth of southwest Japan, within ~20° of profile A′A (Figs. 1, 3). For the migration model we combined a scaled version of the P tomography velocity model of [1,5] with the higher resolution model of [30] in the upper ~500 km, which we specified on a 10 km grid along the cross-section A′A (Fig. 3). Below 500 km we used a scaled model of [1,5]. The resulting P-velocity model was smoothed and the *iasp91* model used as the 1D reference to give absolute velocities. The S model using the *iasp91* V_s/V_p ratios and the P-tomography fluctuations scaled by 2. The data were first band-pass filtered from 0.02–0.25 Hz, then depth migrated trace by trace correcting for out of plane propagation [28]. Following migration each partial image was dip-filtered to eliminate S wave dips greater than 55° from the P wave incident at each scattering point, and then the partial images were summed. The final image is shown in Fig. 5.

3. Results and discussion

In general, the 410- and 660-km discontinuities can be identified easily from the CCP stacks and the migrated receiver function image. The measured depths of the two discontinuities and the corresponding transition zone thickness are shown in Fig. 6. The most distinct anomaly seen in the 410-km topographic map is the high along the 400 km contour of the Wadati–Benioff zone (Fig. 6a). The ridge-like anomaly has a width of ~100–200 km with a topographic relief of ~10–20 km, and stands out prominently in the migrated image. In contrast, the 660-km discontinuity is a very broad topographic low, >400 km, with an amplitude of ~20 km west of the 500 km contour of the seismogenic zone, the approximate maximum depth of seismicity in this region (Fig. 6b). The anomaly is observed under almost all of southwestern Japan and may extend further to the west. The transition zone thus shows significant thickening beneath southwestern Japan with peak amplitude of ~40 km along the 500 km seismicity contour.

The different features in the scales of the anomalies observed at the two discontinuities provide important information for understanding deep subduction processes. From the migrated image we attribute slab penetra-

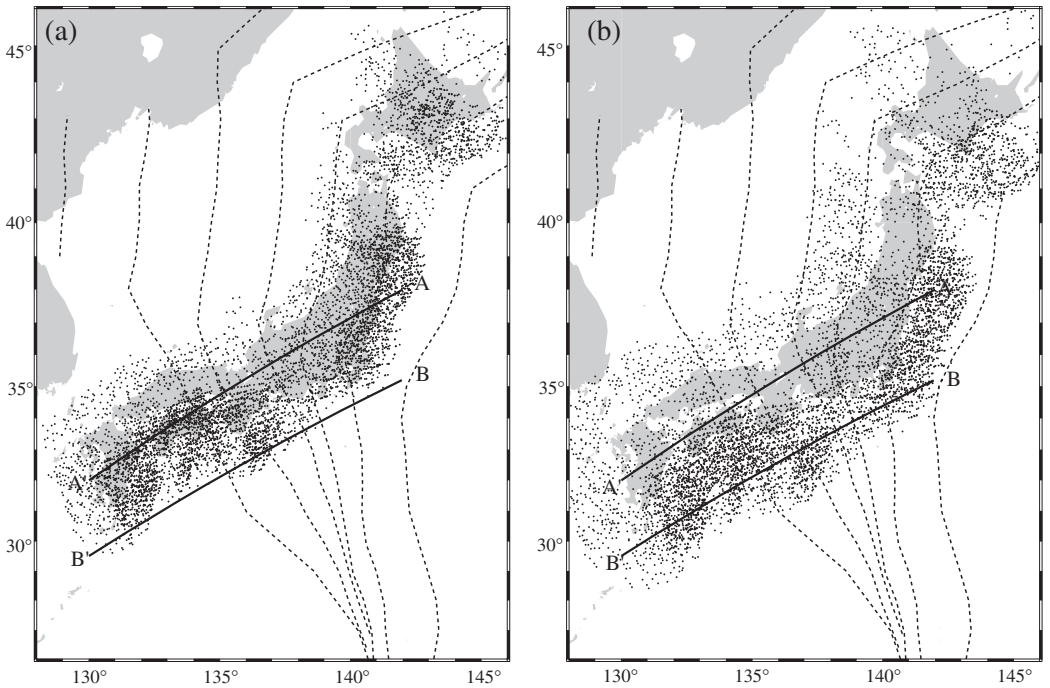

Fig. 3. Geographic distribution of the P to S conversion points at the 410-km discontinuity (a) and 660-km discontinuity (b).

tion as the cause of the narrow anomaly seen at the 410-km, and a flat lying slab as the origin of the broad depression found on the 660-km, since the top of the slab is clearly decreasing in dip and flattening against the base of the transition zone (~550 km depth). Our observations of the 660-km discontinuity are thus consistent with some of the global tomographic images showing a subhorizontal high velocity anomaly around the 660-km discontinuity in the same area [1–5]. Global tomographic images suggest that the entire transition zone is occupied by slab material, presumably cold, however the CCP stacks and the migration image indicate a normal 410-km discontinuity in most of southwestern Japan, except the sharp elevation in the 410 we observe near the point where the slab enters the transition zone. These discrepancies are probably caused by the low depth resolution of the global tomographic images. We also want to emphasize that our observations here agree well with the SS precursor results for this region [9], which showed a broad depression in the 660-km but no resolvable deflection of the 410-km.

The deflected slab could result from two different scenarios. Some workers [31,32] have suggested that a shallow dip angle associated with rapid retrograde trench migration could result in a flat lying slab when it encounters the resistance due to the negative Clapeyron slope of the postspinel phase transition and the abrupt increase in viscosity at the base of the transition zone even in a one-layered convection system. In this case, the deflected slab is still negatively buoyant and will eventually sink into the lower mantle. On the other hand, if the subducting slab undergoes significant deformation, it can begin to fill up the entire transition zone. The large deformation implies either strong resistance from the lower mantle or a buoyant slab at the transition zone depths. In this case, slabs may never enter the lower mantle. We prefer the former interpretation since we don't see slab stacking in the transition zone.

For more detail in the variations of the two discontinuities under southwestern Japan, we show CCP stacks along two profiles AA′ and BB′ that are separated from each other by 3° in Fig. 4a and b, respectively, and in the migration of Fig. 5. Along the north section AA′, in addition to the broad and moderate deepening of the 660-km discontinuity to 680, we also observe a trough ~40 km in amplitude and ~400 km in width. This is consistent with the observations in northeast China by Ai et al. [15] and Li and Yuan [16]. Both studies found significant topography of the 660-km discontinuity within a relatively small area (Fig. 1). This small-scale anomaly was interpreted as evidence of possible penetration into the lower mantle of the deflected slab. Li and Yuan [16] further proposed a model to explain the observed broad depression plus the narrow trough in the 660-km discontinuity. They suggested that the

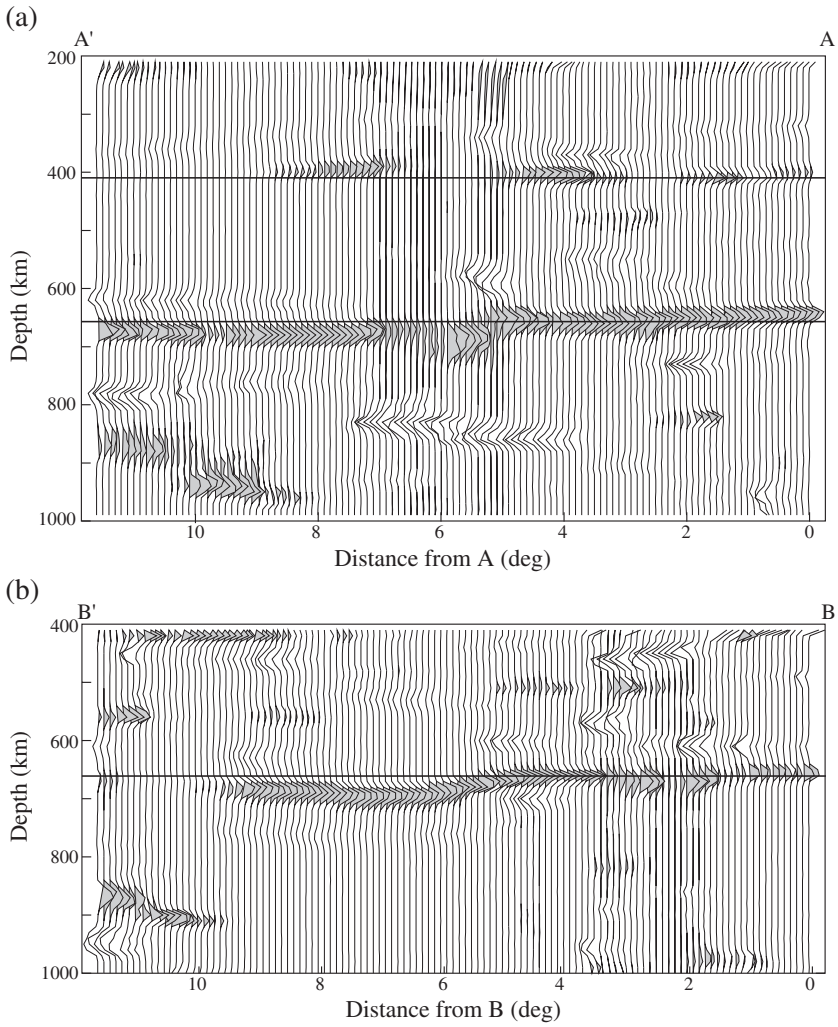

Fig. 4. Two profiles of the CCP gathered receiver functions along the lines AA′ (a) and BB′ (b) from Fig. 1a. The two horizontal lines in (a) indicate P to S conversions at depths of 410 and 660 km. Because of the lack of conversion coverage shallower than 400 km along BB′ (Fig. 3b), stacked waveforms are shown only for the depth range of 400–1000 km.

narrow trough is caused by slab material dripping from the bottom of the slab and penetrating the 660-km. The dynamic feasibility of this dripping mode of subduction is, however yet to be tested. An alternative explanation for the observed 660-km discontinuity structure is the lateral temperature variation within the subducting slab. Slab materials are expected to be colder near the bending part compared to flat area, resulting in the slab separation, as observed in the P tomography of Zhao et al. [30]. Further numerical modeling of the temperature within subducting slabs is required to test this hypothesis.

The P to S conversion also appears to spread in a broader depth range within the trough compared to the other parts of the section (Fig. 4a). Since we used 3D velocity models to calculate the travel times corrections for the CCP stacking, this broader transition may reflect the true structure associated with complicated phase transitions within the slab [11,15]. However, here we must admit that the observations and interpretations of the multi-discontinuity structure are still very controversial. It is possible that the complication is due to out-of-phase gathering.

Along AA′, we see large amplitude variations of P to S conversion at the 410-km discontinuity, which appears as an intermittent structure in both the CCP stacks and the migration. This could reflect the true feature of the discontinuity but it may be a signal-to-noise ratio issue near the southwestern edge of our array. In addition to the two discontinuities, we also see some P to S conversions at depths of ~800–1000 km at the west edge of the section and a strong con-

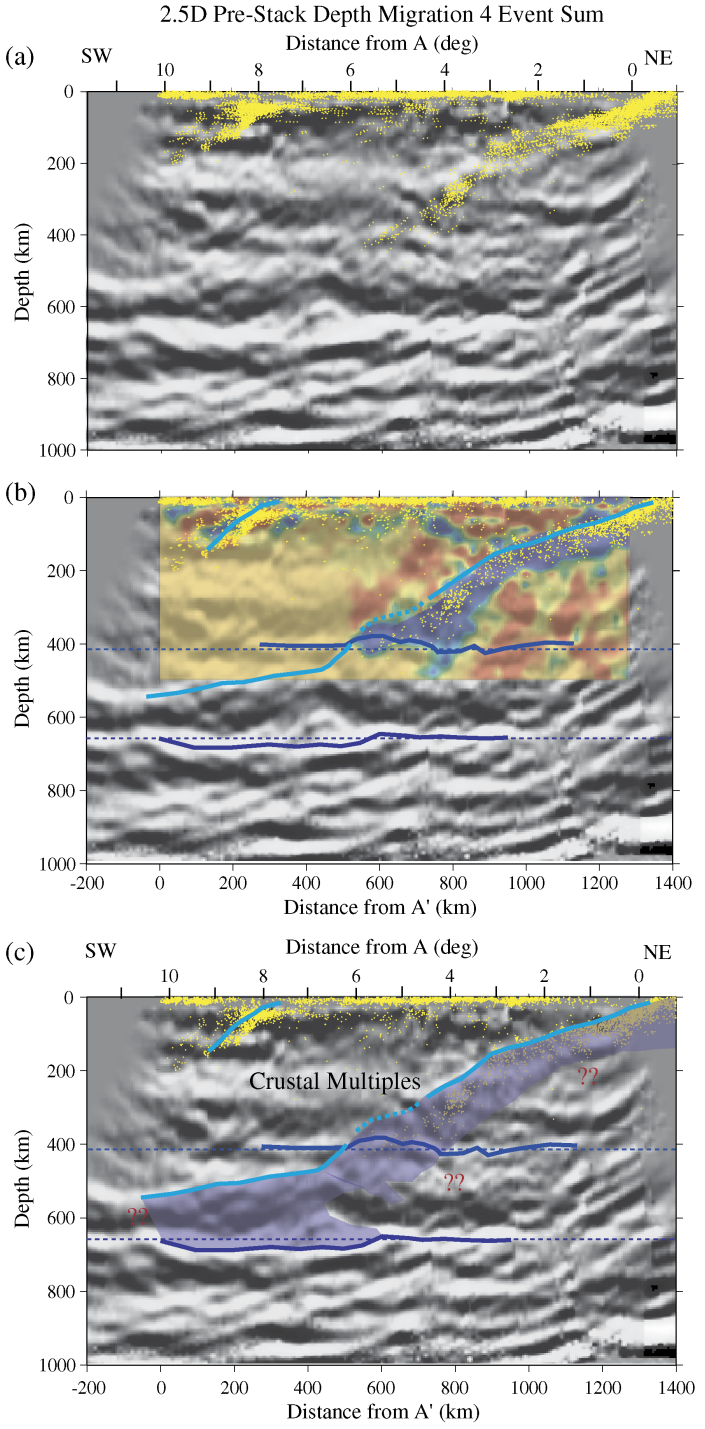

Fig. 5. Pre-stack receiver function depth migration along profile A′A. (a) The migration image is shown with local seismicity overlain. (b) The migration image is shown with seismicity, the 2D P-velocity model of Zhao et al. [30], and interpretation of the top of the slab and the transition zone discontinuities. (c) The migration is shown with an interpretation of secondary events and possible slab structure.

version below the trough in the 660-km in both the CCP stacks and the migration. We used a variety of subsets of the CCP data to test the robustness of these signals [33] and found that they show up in all cases in the CCP stacks. Thus they are likely real structures, although we don't know how to interpret them. If they

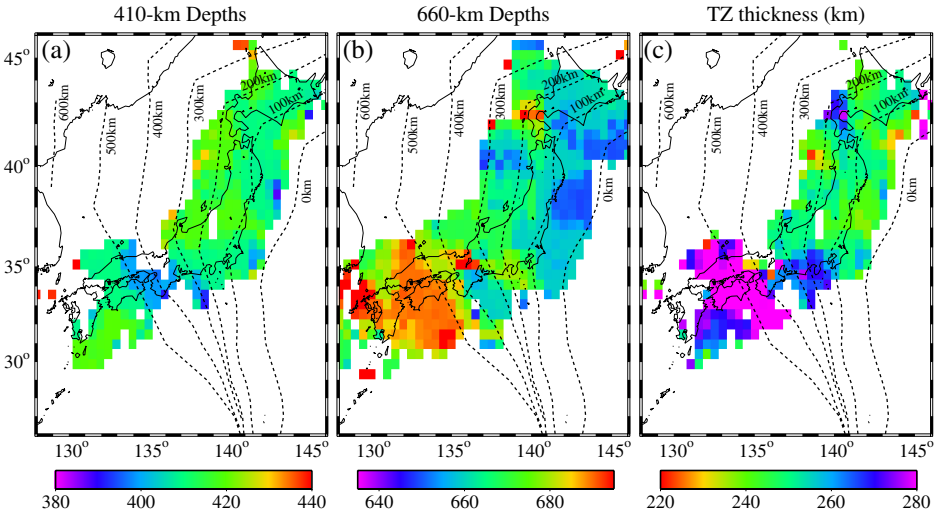

Fig. 6. Map view of (a) the depth to the 410-km discontinuity, (b) the depth to the 660-km discontinuity, and (c) mantle transition-zone thickness. The depth to the Wadati–Benioff zone is shown by the dashed lines.

are structure related to the subducting slab as observed beneath the Marianas [34,35] and Indonesia [36], then they could be the manifestation of the presence of slab in the uppermost lower mantle in this region.

We could not find a systematic P to S conversion generated at the upper boundary of the subducting slab from our CCP gathers, although it is clearly imaged over parts of the upper mantle in the migration. We believe this is due to the 4th root signal enhancing technique that we used here, which suppresses dipping energy. As in reflection seismology, CCP stacking is suitable for resolving horizontally layered structures, while migration techniques provide better images of dipping structures like the subducting slab.

4. Conclusions

In this study, we have demonstrated that receiver function analysis is applicable to short-period seismic networks. We were able to identify P to S conversions at the two mantle discontinuities from the 4th root CCP stacks of receiver functions and the pre-stack depth migrated receiver functions. We have focused on southwestern Japan to capitalize on the high data density in order to study the influence of the subducting Pacific slab on the transition zone discontinuities. We found both discontinuities are affected by the subducting slab, but in very different ways. We observed a narrow uplift of the 410-km and a broad depression of the 660-km beneath the southwestern Japan in the CCP stacks and the migration image. These observations are consistent with the receiver-functions images made in the northeastern China over the same subduction zone, and also agree with global tomographic images of a flat lying slab in this region. Whether part of this deflected slab is sinking into the lower mantle is not constrained by our observations. Also since the seismic network is only in Japan, it is impossible to constrain the western part of the 660-km discontinuity where it is deepening. Future large-scale seismic deployments in the Korean Peninsula and northeastern China are required to better image three dimensional structures of the subducting slabs in the northwestern Pacific which is vital to better understanding of deep subduction processes.

Acknowledgments

We thank the National Research Institute for Earth Science and Disaster Prevention of Japan for providing the Hi-net data. We thank S. King, J. Ritsema and two anonymous reviewers for critical and constructive reviews. This work was supported by the Department of Earth Science, Rice University (Niu), NSF CMG grant EAR-0222270 (Ham, Levander) and the Japan Marine Science and Technology Center (Obayashi).

References

[1] Y. Fukao, M. Obayashi, M. Inoue, M. Nenbai, Subducting slabs stagnant in the mantle transition zone, J. Geophys. Res. 97 (1992) 4809–4822.
[2] H.-W. Zhou, A high resolution P wave model for the top 1200 km of the mantle, J. Geophys. Res. 101 (1996) 27791–28710.
[3] R.D. van der Hilst, S. Widiyantoro, E.R. Engdahl, Evidence for deep mantle circulation from global tomography, Nature, 386 (1997) 578–584.

[4] H. Bijwaard, W. Spakman, E.R. Engdahl, Closing the gap between regional and global travel-time tomography, J. Geophys. Res. 103 (1998) 30,055–30,078.
[5] Y. Fukao, S. Widiyantoro, M. Obayashi, Stagnant slabs in the upper and lower mantle transition zone, Geophys. Rev. 39 (2001) 291–323.
[6] A.W. Hofmann, Mantle geochemistry: the message from oceanic volcanism, Nature 385 (1997) 219–229.
[7] E. Ito, E. Takahashi, Postspinel transformations in the system $Mg_2SiO_4Fe_2SiO_4$ and some geophysical implications, J. Geophys. Res. 94 (1989) 10,637–10,646.
[8] P.M. Shearer, T.G. Masters, Global mapping of topography on the 660 km discontinuity, Nature 355 (1992) 791–796.
[9] M.P. Flanagan, P.M. Shearer, Global mapping of the topography on the transition zone velocity discontinuities by stacking SS precursors, J. Geophys. Res. 103 (1998) 2673–2692.
[10] F. Neele, H. De Regt, J. VanDecar, Gross errors in upper-mantle discontinuity topography from underside reflection data, Geophys. J. Int. 129 (1997) 194–204.
[11] P.M. Shearer, M.P. Flanagan, M.A.H. Hedlin, Experiments in migration processing of SS precursor data to image upper mantle discontinuity structure, J. Geophys. Res. 104 (1999) 7229–7242.
[12] F. Niu, H. Kawakatsu, Complex structure of the mantle discontinuities at the tip of the subducting slab beneath the northeast China: a preliminary investigation of broadband receiver functions, J. Phys. Earth 44 (1996) 701–711.
[13] F. Niu, H. Kawakatsu, Determination of the absolute depths of the mantle transition zone discontinuities beneath China: effect of stagnant slabs on transition zone discontinuities, Earth Planets Space 50 (1998) 965–975.
[14] P. Vacher, A. Mocquet, C. Sotin, Computation of seismic profiles from mineral physics: the importance of the non-olivine components for explaining the 660 km depth discontinuity, Phys. Earth Planet. Inter. 106 (1998) 277–300.
[15] Y. Ai, T. Zheng, W. Xu, Y. He, D. Dong, A complex 660-km discontinuity beneath northeast China, Earth Planet. Sci. Lett. 212 (2003) 63–71.
[16] X. Li, X. Yuan, Receiver functions in northeast China implications for slab penetration into the lower mantle in northwest Pacific subduction zone, Earth Planet. Sci. Lett. 216 (2003) 679–691.
[17] C.A. Langston, Structure under Mountain Rainer, Washington, inferred from teleseismic body waves, J. Geophys. Res. 84 (1979) 4749–4762.
[18] L.P. Vinnik, Detection of waves converted from P to SV in the mantle, Phys. Earth Planet. Inter. 15 (1977) 39–45.
[19] R.W. Clayton, R.A. Wiggins, Source shape estimation and deconvolution of teleseismic body waves, Geophys. J. R. Astr. Soc. 47 (1976) 151–177.
[20] C.J. Ammon, The isolation of receiver effects from teleseismic P waveforms, Bull. Seismol. Soc. Am. 81 (1991) 2504–2510.
[21] K. Aki, P.G. Richards, Quantitative Seismology: Theory and Methods, W.H. Freeman and Co., San Francisco, CA, 1980.
[22] K.G. Dueker, A.F. Sheehan, Mantle discontinuity structure from midpoint stacks of converted P and S waves across the Yellowstone hotspot track, J. Geophys. Res. 102 (1997) 8313–8328.
[23] Y. Shen, S.C. Solomon, I.Th. Bjarnason, C.J. Wolfe, Seismic evidence for a lower-mantle origin of the Iceland plume, Nature 395 (1998) 62–65.
[24] F. Niu, A. Levander, C.M. Cooper, C.-T.A. Lee, A. Lenardic, D.E. James, Seismic constraints on the depth and composition of the mantle keel beneath the Kaapvaal craton, Earth Planet. Sci. Lett. 224 (2004) 337–346.
[25] B.L.N. Kennett, E.R. Engdahl, Travel times for global earthquake location and phase identification, Geophys. J. Int. 105 (1991) 429–465.
[26] K.J. Muirhead, Eliminating false alarms when detecting seismic events automatically, Nature 217 (1968) 533–534.
[27] E.R. Kanasewich, Time Sequence Analysis in Geophysics. Edmonton, AB: University of Alberta Press, Edmonton, AB, 1973, 364 pp.
[28] A. Levander, F. Niu, W.W. Symes, Imaging teleseismic P to S scattered waves using the Kirchhoff integral, in: A. Levander, G. Nolet (Eds.), Array Analysis of Broadband Seismograms, Washington D.C.: American Geophysical Union, 2005, pp. 149–170.
[29] A. Levander, F. Niu, C.-T.A. Lee, Xin Cheng, Imag(in)ing the continental lithosphere, Phys. Earth Planet. Inter., in press.
[30] D. Zhao, A. Hasegawa, H. Kanamori, Deep structure of Japan subduction zone as derived from local, regional, and teleseismic events, J. Geophys. Res. 99 (2005) 22,313–22,329.
[31] U.R. Christensen, The influence of trench migration on slab penetration into the lower mantle, Earth Planet. Sci. Lett. 140 (1996) 27–39.
[32] S. Zhong, M. Gurnis, Dynamic interaction between tectonic plates, subducting slabs, and the mantle, Earth Interact. 1 (1997) 1–18.
[33] B. Efron, R. Tibshirani, Bootstrap methods for standard errors, confidence intervals, and other measures of statistical accuracy, Stat. Sci. 1 (1986) 54–75.
[34] S. Kaneshima, G. Helffrich, Subparallel dipping heterogeneities in the mid-lower mantle, J. Geophys. Res. 108 (2003), doi:10.1029/2001JB001596.
[35] F. Niu, H. Kawakatsu, Y. Fukao, A slightly dipping and strong seismic reflector at mid-mantle depth beneath the Mariana subduction zone, J. Geophys. Res. 108 (2003) 2419, doi:10.1029/2002JB002384.
[36] F. Niu, H. Kawakatsu, Depth variation of the mid-mantle seismic discontinuity, Geophys. Res. Lett. 24 (1997) 429–432.